Li, Xiuxiu; Yang, Song; Wang, Jun; Lund, Peter

High-temperature two-layer integrated receiver storage for concentrating solar power systems

Published in:
Oxford Open Energy

DOI:
10.1093/ooenergy/oiac012

Published: 01/01/2023

Document Version
Publisher's PDF, also known as Version of record

OXFORD

Oxford Open Energy, 2023, **2**, 1–13
https://doi.org/10.1093/ooenergy/oiac012
Advance access publication date 12 December 2022
Research Article

High-temperature two-layer integrated receiver storage for concentrating solar power systems

Xiuxiu Li[1], Song Yang[2,*], Jun Wang[1] and Peter D. Lund[1,3]

[1]School of Energy and Environment, Southeast University, Nanjing, 210096, China
[2]School of Chemical Engineering, University of Birmingham, Birmingham B15 2TT, UK
[3]Aalto University School of Science, Aalto, 00076, Finland
*Correspondence address. School of Chemical Engineering, University of Birmingham, Birmingham B15 2TT, UK. E-mail: s.yang.5@bham.ac.uk

Abstract

An integrated receiver storage for a beam-down concentrating solar power (CSP) plant enables simplifying the system layout and reducing the costs. Here a two-layer integrated receiver storage (TLIRS) system design is proposed consisting of a cavity receiver and a two-layer packed-bed storage. The first layer is a porous ceramic and the second one is rocks. To enable performance optimization of the system, models for cavity radiation, two-phase transient heat transfer and local thermal nonequilibrium were derived and validated. The thermal performance of the TLIRS system was assessed and characterized by the absorbing, charging, discharging and overall efficiencies and by the solar-to-exergy conversion ratio. The results indicate that the porous ceramic layer significantly enhances the absorption of solar irradiance and thus improves the thermal efficiencies. For CSP applications, the TLIRS system potentially achieves high thermal performance in repetitive charging and discharging cycles.

Graphical Abstract

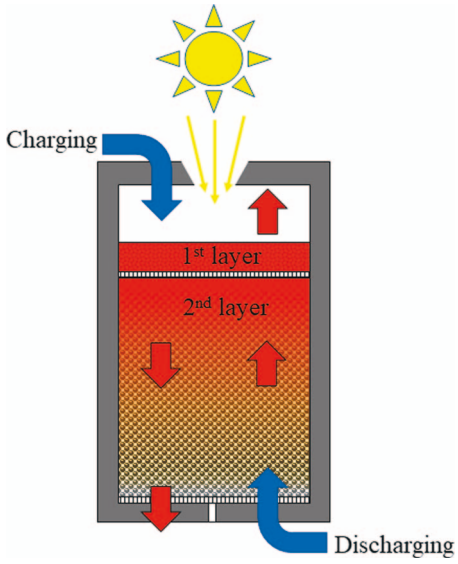

Keywords: thermal efficiency, packed bed, porous ceramic, concentrating solar power

INTRODUCTION

Mitigation of climate change is a major challenge for the societies, requiring elimination of most energy-based emissions in the coming decades. Renewable energy is perceived as one of the key strategies to reach carbon neutrality. IEA estimates that e.g. solar and wind together could stand for 70% of all electricity by 2050. Solar energy could contribute by more than 20% of the total energy production already by 2040 [1, 2] and it is perceived as one of the most promising future energy technologies [3–5]. Within the solar technologies, concentrating solar power (CSP) is a potential solution for large-scale commercial applications [6–9]. CSP can also be integrated with thermal energy storage (TES) to improve the dispatchability of solar energy [10–12]. There are different

Received: October 16, 2022. **Revised:** November 20, 2022

types of CSP available such as central-tower with a heliostat field or parabolic trough systems. To avoid excessive heat losses when transferring the heat transfer fluid (HTF) between the receiver and storage, an innovative concept integrating the receiver and storage (IRS) [13] coupled to a beam-down tower concentrator [14] has been proposed.

The beam-down CSP has intensively been investigated [14–17]. Compared to the traditional central tower plant, the beam-down system provides several benefits: i) installation and maintenance is easier and more cost-effective through moving the receiver on ground instead of off-ground; ii) avoiding thermal losses in the HTF circuit from the receiver to the storage tank; iii) reduced height of the central tower can lead to a higher solar concentration ratio [18]. The solar beam-down system has been integrated with a range of applications, e.g. for thermochemical fuel production [19–25]. So far, three beam-down demonstration plants for thermochemical applications [26] and one commercial CSP plant for power generation [27] has bee realized.

The physical designs for the IRS system differ somewhat in the way heat-receiving, charging and discharging has been realized [26, 28–30]. An IRS system can be fluidized bed or packed-bed, based on the heat transfer and storage materials employed. Examples of past work on fluidized-bed IRS systems include, e.g. the concept of 'CSPonD' consisting of a volumetric absorption molten salt receiver with integral storage proposed [13], a preliminary design of a tank/receiver for a 100-kW_{th} beam-down on-sun plant [28] and a demonstration direct absorption molten salt receiver for CSP [31]. In fluidized-bed systems, the temperature limitations of common molten salts, e.g. sodium–potassium nitrate, for use as heat transfer and storage material have limited the operational range to 220°C to 590°C [13]. On the contrary, packed-bed IRS using solid storage materials and gaseous heat transfer medium possess a much broader operating temperature range. For instance, sand-basalt beds were employed in a novel heat storage system. Simulation of such system yielded utilization factors from 0.53 to 0.73 [26]. Yang *et al.* proposed a design of a cavity receiver combined with a thermocline heat storage yielding a high solar-to-exergy conversion ratio of 0.52 using an optimized design [29, 30].

In this study, a novel two-layer IRS system design is proposed, which consists of a porous ceramic receiver and a rock-bed storage. Ceramic materials are good candidates as high-temperature heat transfer medium due to hardness, chemical inertness, resistance to oxidizing atmospheres, high melting point, corrosion and wear resistance, low density, low thermal expansion and high thermal shock resistance [32, 33]. Porous structures of large specific surfaces also enhance heat transfer in heat-intensive applications [34, 35] and has also been used as solar absorber material [36]. Silicon carbide-based ceramics have successfully been employed for high-temperature applications due to their superior thermal properties [37]. In addition, using rocks as storage material and air as HTF is due to low cost, ample abundance, no hazardous or corrosive ingredient, direct heat transfer, etc [38]. However, the research literature on combining porous ceramic and packed bed is very limited. The present work therefore intends to provide new insight to a two-layer integrated receiver storage (TLIRS) system for a beam-down CSP system, which could improve the thermal performance and simplify the operation and overall design of such systems.

The paper is organized as follows. The geometric structure and the operating approach of the new system are given in Section 2 followed by the heat transfer modeling of the critical components and definition of thermal performance indicators in Section 3. In Section 4, the main results are presented, including temperature behavior of air and beds and the impact of air mass flow rate on the system thermal performance. In addition, the thermal performance of the new system is compared to a single-layer integrated receiver storage (SLIRS) and other CSP plants. The paper ends with conclusions.

DESCRIPTION OF THE TWO-LAYER INTEGRATED RECEIVER STORAGE SYSTEM

The details of geometric structure, materials and operating method of the TLIRS system are presented in the next. The TLIRS reference system used here is 500 kW beam-down CSP plant. A schematic of the working principle is in Fig. 1 with the main parameters given in Table 1.

The cylindrical system in Fig. 1 includes the cavity receiver and the packed-bed storage body with the inner radius of R_2 and a total height of $H_1 + H_2 + H_3$. The cavity receiver of aperture R_1 is above the ground and has a height of H_1. Its insulation contains two layers: Al_2O_3–SiO_2 (inner) and Foamglas® (outer), with a total thickness of L_1. The outermost coating of the receiver is a thin layer of Inconel 600. The packed bed of height H_3 is immersed in the ground to reduce the lateral pressure and insulation. It consists of two layers: The porous ceramic layer with a height of H_2 made of siliconized silicon carbide (SSiC) is used to strengthen heat transfer. The second layer is a layer of rocks containing siliceous limestone, quartzite, limestone, calcareous sandstone and gabbro with the equivalent thermal properties and geometries. The packed bed is wrapped up with insulation (Microtherm®, Foamglas®) and concrete (ultra high-performance concrete and low-density concrete). The total thickness of the base and side is L_2. Table 2 gives the main physical properties of the materials in the system.

The compound paraboloid concentrator is mounted above the aperture of the cavity to improve the concentration ratio. The sidewalls of the cavity have four evenly distributed air outlets pipes (not all shown in Fig. 1) to reduce the influence of air that bypasses in the discharging stage. Metal meshes are placed under the porous ceramic layer and at the bottom of beds to eliminate the heterogeneity of flow velocity at the same cross-section. A fan is mounted at the bottom to drive the air flow. In order to ensure the continuous operation of the IRS system, the working time of each cycle is set to 24 hours. Considering the local sunshine conditions, the charging time is set as 8 hours (28 800 seconds), and the discharging time is set as 16 hours (57 600 seconds). The local solar irradiance within 8 hours of daytime is high enough to facilitate heat storage, so the rest of the time is set as the discharging stage. The operating process of the two stages is as follows: (i) during the charging stage, the porous ceramic layer is exposed to concentrated solar irradiance to be heated up during the charging stage. With the help of a fan, air enters the IRS system from the open aperture, flows downward through the beds and finally exits from the bottom. The descending flow enhances heat transfer from the upper layer to the rest of the storage; (ii) during the discharge stage, air flows through the beds reversely and approaches the maximum temperature before exiting the outlets on the cavity sidewalls. The aperture is plugged to avoid leakage of hot air.

NUMERICAL MODELING OF THE SYSTEM

To analyze and optimize the thermal performance of the TLIRS system, we developed decoupled heat transfer models for the cavity receiver and the packed beds with two layers (porous ceramic

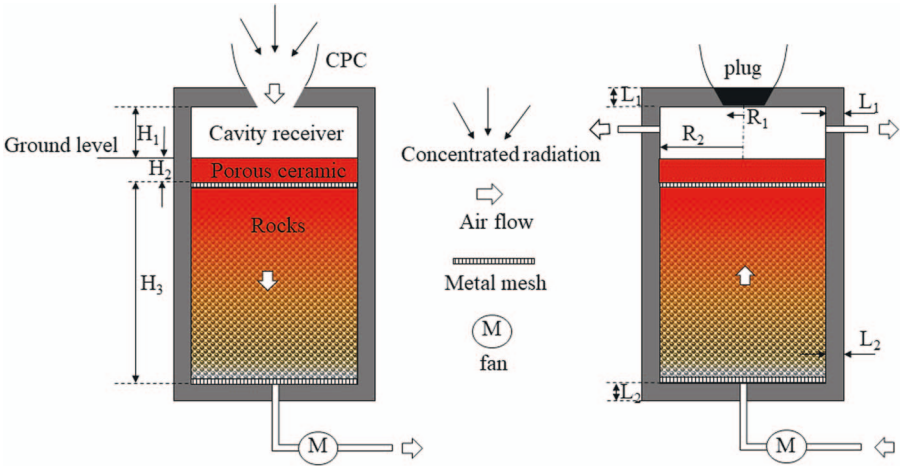

Figure 1. Scheme of the TLIRS system configuration.

Table 1. Dimensions and operating conditions of the TLIRS system design

Dimensions		**Operating conditions**	
H_1 (m)	**1.5**	**Charging time, t_{ch} (s)**	**28 800**
H_2 (m)	0.1	Discharging time, t_{dis} (s)	57 600
H_3 (m)	8	cycle number, n (–)	30
R_1 (m)	0.447	HTF's mass flow rate during charging, $\dot{m}_{ch}$ (kg s^{-1})	0.3 ~ 0.9
R_2 (m)	2	HTF's mass flow rate during discharging, $\dot{m}_{dis}$ (kg s^{-1})	0.15 ~ 0.45
L_1 (m)	0.7	Incident radiation flux, $\dot{Q}_{inc}$ (kW)	439.8
L_2 (m)	1.82	Initial temperature, T_0 (K)	298
d_{pc} (m)	0.00003	Ambient temperature, T_∞ (K)	298
ε_{pc} (–)	0.4	Efficiency of fan, η_{fan} (–)	0.95
d_s (m)	0.03	Solar-to-power efficiency of commercial CSP plant, η_{CSP} (–)	0.23
ε_s (–)	0.4		

and rock layer). Main assumptions employed in the modeling are given as follows:

- a plug flow is considered so that the air mass flow rate is uniform at any cross-section perpendicular to the packed beds;
- radial temperature differences in the beds are ignored;
- for the discharging stage, conductive heat losses at the cavity walls are ignored;
- the porosity of porous ceramic is uniform and isotropic;
- the thermal inertia of the porous ceramic layer is neglected and thus a steady-state heat transfer model is employed;
- the physical properties of porous ceramics are independent of temperature;
- the heat transfer between the two layers is dominated by convection.

Cavity receiver

The cavity receiver is a critical component of the photothermal conversion process in the solar power system. The heat transfer mechanism of the cavity receiver in IRS system proposed by Yang *et al.* [29] is shown in Fig. 2.

Monte Carlo ray-tracing is used to obtain the matrix of the view factor of the cavity inner walls. The inner surface of the receiver is meshed, and the expression of the total number of discrete grids N is shown in Eq. (1)

$$N = N_r N_f + N_z N_f \tag{1}$$

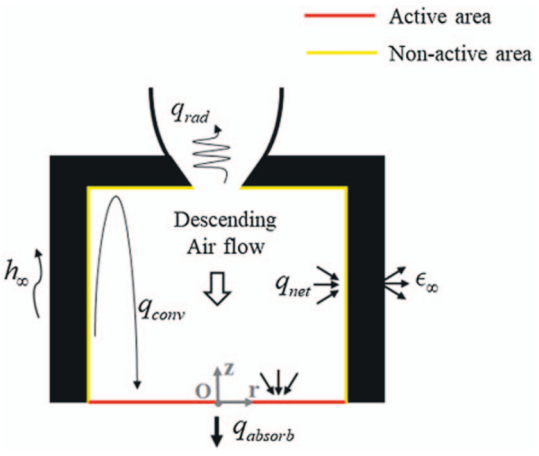

Figure 2. The heat transfer mechanism of the cavity receiver [29]

where the number of nodes in radial direction N_r, axial direction N_z and circumferential N_f direction are set to 50, 20 and 20, respectively.

The view factor matrix F on the inner surface of the cavity is an $N \times N$ two-dimensional matrix, which is used to store the view factors between each grid, as shown in Eq. (2):

$$F_{kj} = N_j / N_k \tag{2}$$

Table 2. Main physical properties of porous ceramic, rocks and air in the TLIRS system

Material	Conductivity and Specific Heat and Viscosity and Density and Emissivity k (W m^{-1} K^{-1}) and c_p (J kg^{-1} K^{-1}) and ν ($\times 10^6$ m^2 s^{-1}) and ρ (kg m^{-3}) andϵ (–)
Porous ceramic [39]	$k_{pc} = 100$
Rocks [38, 40–42]	$k(T) = \begin{cases} k_{20} - A(T-B)(k_{20}-C)\left[k_{20}(DT)^{-Ek_{20}} + F\right]k_{20}^{-G} & k_{20} > 2 \\ k_{20} - A(T-B)(k_{20}-C) & k_{20} < 2 \end{cases}$ $c_p(T) = 747.0995 + 0.5676 \times (T - 273)$ $\rho = 2732.6$ $\epsilon = 0.85$
Air [43, 44]	$k_f = 2.35 \times 10^{-12}T^3 - 1.290 \times 10^{-8}T^2 + 4.8370613 \times 10^{-5}T + 0.00483$ $c_{p,f} = 1171 \times e^{-\left(\frac{T-3070}{2257}\right)^2} + 691.6 \times e^{-\left(\frac{T-516.2}{1673}\right)^2} + 191 \times e^{-\left(\frac{T+114.3}{399.4}\right)^2}$ $\nu_f = 258.7 - 259.4\cos(0.001214T) - 88.17\sin(0.001214T) - 6.35\cos(0.002428T) + 49.59\sin(0.002428T) - 5.995\cos(0.003642T) - 0.2957\sin(0.003642T)$ $\rho_f = 352.6T^{-0.9998} - 1.747 \times 10^{-4}$
Al_2O_3-SiO_2 [45]	$k(T) = 0.00012926T + 0.019654$ $c_p(T) = \min\left\{4 \times 10^{-7}T^3 - 1.3797 \times 10^{-3}T^2 + 1.5987289T + 477.6995948, 1118.44\right\}$ $\rho = 560.65$ $\epsilon = 0.85$
Insulation [42]	$k = 0.025/0.05/2.05/0.375/0.5$(*Microtherm®/Foamglas®/UPC/LDC/Soils*)$c_p = 840$(*Foamglas®*) $\rho = 115$(*Foamglas®*) $\epsilon(T) = 0.0001982 \times T + 0.5734$(*Inconel* 600)

where k and j are the k^{th} and j^{th} grids of the internal surface of the cavity, respectively.

F_{kj} is the view factor of the k^{th} discrete plane element to the jth discrete plane element.

Considering the calculation speed and accuracy, the total ray emission quantity is 1×10^8.

The radiosity method was used to get the net irradiance flux at the cavity bottom:

$$\sum_{j=1}^{N}\left(\delta_{kj} - \left(1-\epsilon_j\right)F_{kj}\right)\frac{q_{net,j}}{\epsilon_j} = q_{inc,j} - \sum_{j=1}^{N}\left(\delta_{kj} - F_{kj}\right)\sigma T_j^4 \tag{3}$$

where $q_{inc,j}$ and $q_{net,j}$ represent the incident solar irradiance and the net radiative heat flux at the jth grid. T_j is the cavity wall temperature at the jth grid. δ_{kj} is the Kronecker function. When k and j are positive integers, the expressions are shown in Eq. (4)

$$\delta_{kj} = \begin{cases} 1 & k = j \\ 0 & k \neq j \end{cases} \tag{4}$$

The absorbing heat flux q_{absorb} at the bottom of the cavity is the difference between the net radiative heat flux q_{net} and the heat loss q_{loss}, which was fitted as a three-order polynomial function of the temperature.

$$q_{absorb}(T) = AT^3 + BT^2 + CT + D \tag{5}$$

where A, B, C and D are equal to -1.246×10^{-5}, 0.0148, −7.434 and 3.572×10^4. T is the temperature at the bottom of the cavity receiver.

Porous ceramic layer

The porous ceramic layer is arranged at the top of the beds and separated with the layer of rocks by using the metal mesh. Then, the upper surface of the layer is exposed directly to the solar irradiance. The local thermal nonequilibrium method is used to model the heat transfer of fluid and solid phases in the domain of the porous ceramic layer [46]:

Fluid:

$$a_s\dot{m}_{ch}\frac{\partial\left(c_{p,f}T_f\right)}{\partial z} = h_v\left(T_{pc} - T_f\right) \tag{6}$$

Solid:

$$0 = \frac{\partial}{\partial z}\left(k_{eff,pc}\frac{\partial T_{pc}}{\partial z}\right) + h_{v,pc}\left(T_f - T_{pc}\right) + \frac{\partial}{\partial z}\left(k_{rad}\frac{\partial T_{pc}}{\partial z}\right) \tag{7}$$

where the effective thermal conductivity of the porous ceramic and air are calculated by [47].

$$k_{eff,pc} = \left(1 - \varepsilon_{pc}\right)k_{pc} \tag{8}$$

The Rosseland diffusion approximation is used to approximate radiative heat transfer by treating it as a diffusion process similar to Fourier conduction [48]. k_{rad} is the equivalent radiation heat transfer coefficient calculated by:

$$k_{rad} = \frac{16n^2\sigma T_{pc}^3}{3\beta} \tag{9}$$

$$\beta = \frac{3\left(1 - \varepsilon_{pc}\right)}{d_{pc}} \tag{10}$$

where n is the refractive index assumed to be 1 because the primary path of radiation is through the gas filled pores [49, 50]. The extinction coefficient for porous ceramic is 60 000 m^{-1} in this paper by solving Eq. (10), resulting in an optical thickness much greater than 1, so the Rosseland diffusion approximation is expected to be applicable [51–54].

The volumetric heat transfer coefficient is calculated using the model of Hwang *et al.* [55] and Alazmi and Vafai [56]:

$$h_{v,pc} = h_{sf}\alpha_{sf} \tag{11}$$

$$h_{sf} = 0.004\left(d_v/d_{pc}\right)^{0.35}\left(k_f/d_{pc}\right)Pr^{0.33}Re^{1.35} \quad \mathrm{Re} \leq 75 \tag{12}$$

$$h_{sf} = 1.064\left(k_f/d_{pc}\right)Pr^{0.33}Re^{0.59} \quad \mathrm{Re} \geq 350 \tag{13}$$

Note that, for 75 < Re < 350, the interpolation method was used to solve h_{sf} by Eqs. (9) and (10).

$$\alpha_{sf} = 20.346\left(1-\varepsilon_{pc}\right)\varepsilon_{pc}^2/d_{pc} \tag{14}$$

$$d_v = 4\varepsilon_{pc}/\alpha_{sf} \tag{15}$$

$$\begin{aligned}\textbf{Boundary conditions}: z=0: \quad & T_f = T_\infty, q = q_{absorb}, \partial T_{pc}/\partial z = 0\\ z = H_2: \quad & \partial T_f/\partial z = \partial T_{pc}/\partial z = 0\end{aligned} \tag{16}$$

$$\textbf{Initial conditions}: 0 < z < H_2: \quad T_f = T_{pc} = T_0 \tag{17}$$

For the numerical analysis, the grid independence verification was carried out to determine the grid number in axial. The number is set to 125 after balancing with the cost of central processing unit's time. The second-order central and backward difference methods are used in the equation discretization and Gaussian Seidel iterative method in solving. When maximum temperature relative errors between two iterations are less than 10^{-8}, results are considered to be convergent.

Layer of rocks

The layer of rocks is simulated using a one-dimensional two-phase dynamic heat transfer model. Fluid and solid phases are separately modeled with variable thermophysical properties based on the law of energy conservation Eqs. (18, 19):

$$\textbf{Solid}: \frac{\partial\left(\left(1-\varepsilon\right)\rho_s c_{p,s}T_s\right)}{\partial t} = \frac{\partial}{\partial z}\left(k_{eff}\frac{\partial T_s}{\partial z}\right) + h_v\left(T_f - T_s\right) \tag{18}$$

$$\textbf{Fluid}: \frac{\partial\left(\varepsilon\rho_f c_{p,f}T_f\right)}{\partial t} + \frac{\partial\left(c_{p,f}a_s\dot{m}T_f\right)}{\partial z} = h_v\left(T_s - T_f\right) + U_w C_w\left(T_\infty - T_f\right) \tag{19}$$

The effective conductivity of packed bed, k_{eff}, uses the correlation of Kunii and Smith [57, 58].

$$k_{eff} = k_f\left[\varepsilon\left(1+\beta\frac{h_{rv}d}{k_f}\right) + \frac{\beta\left(1-\varepsilon\right)}{\frac{1}{1/\phi+h_{rs}d/k_f} + 2k_f/3k_s}\right] \tag{20}$$

$$\phi = \phi_2 + \left(\phi_1 - \phi_2\right)\frac{\varepsilon-\varepsilon_2}{\varepsilon_1-\varepsilon_2} \tag{21}$$

$$\phi_i = \frac{\left(k_s-k_f\right)/k_s n_i}{2\ln\left(k_s/k_f - \left(k_s-k_f\right)/k_f\sqrt{1-\frac{1}{n_i}}\right) - 2\left(k_s-k_f\right)\left(1-\sqrt{1-\frac{1}{n_i}}\right)/k_s} - \frac{2k_f}{3k_s}\left(i=1,2\right) \tag{22}$$

$$h_{rv} = \frac{3.4424\sigma {T_f}^3}{1+\varepsilon\left(1-\epsilon_s\right)/2\left(1-\varepsilon\right)\epsilon_s} \tag{23}$$

$$h_{rs} = 3.4424\left(\frac{\epsilon_s}{2-\epsilon_s}\right)\sigma {T_s}^3 \tag{24}$$

where β, ε_1, ε_2, n_1 and n_2 are equal to 0.9, 0.476, 0.26, 1.5 and $4\sqrt{3}$.

h_v is the volumetric heat transfer coefficient between air and rock, which is solved by the model by Alanis *et al.* and Coutier and Farber.

$$h_v = l_m\left(\dot{m}/d\right)^{l_n} \tag{25}$$

where l_m and l_n depend on the Reynolds number (Table 3).

Table 3. Coefficients for volumetric convective heat transfer correlation

	l_m	l_n
Small Reynolds number (<50) [59]	700	0.76
Large Reynolds number (50–400) [60]	824	0.92

The comprehensive heat transfer coefficient of sidewall U_w is the reciprocal of the sum of the thermal resistance between the rock layer (including fluid) and the inner wall and the thermal resistance of the insulation layer.

$$U_w = \frac{1}{1/U_{inside} + R_2\sum_{j=1}^{5}\left(1/k_{w,j}\right)\ln\left(r_{j+1}/r_j\right)} \tag{26}$$

$$U_{inside} = h_{conv,w} + h_{rad-cond,w} \tag{27}$$

$$h_{conv,w} = \frac{k_f}{d}\left[3.22(RePr)^{1/3} + 0.117Re^{4/5}Pr^{2/5}\right] \tag{28}$$

$$h_{rad-cond,w} = \frac{k_{eff,w}}{R_2\ln\left(R_2/\left(R_2-d/2\right)\right)} \tag{29}$$

where j stands for Microtherm®, Foamglas®, ultra high-performance concrete, low density concrete and soil, $j = 1, 2, 3, 4, 5$. r_j and r_{j+1} are the inner diameter and outer diameter of the j^{th} insulation layer. $k_{w,j}$ is the thermal conductivity of the j^{th} insulation layer.

$h_{conv,w}$ and $h_{rad-cond,w}$ accounts for the convection [61] and the radiation-conduction terms, correspondingly. $k_{eff,w}$ in Eq. (29) is obtained from correlations given by Ofuchi and Kunii [62], which is similar to Eq. (20).

Boundary conditions:

$$\begin{aligned}\textbf{Charging}: t>0, z=0: \quad & T_f = T_{outlet,pc},\ \partial T_s/\partial z = 0\\ t>0, z=H_3: \quad & \partial T_f/\partial z = \partial T_s/\partial z = 0\end{aligned} \tag{30}$$

$$\begin{aligned}\textbf{Discharging}: t>0, z=0: \quad & \partial T_f/\partial z = \partial T_s/\partial z = 0\\ t>0, z=H_3: \quad & T_f = T_\infty,\ \partial T_s/\partial z = 0\end{aligned} \tag{31}$$

$$\textbf{Initial conditions}: t=0, 0<z<H_3: \quad T_f = T_s = T_0 \tag{32}$$

Definition of thermal performance indicators

The absorbing efficiency, charging efficiency, discharging efficiency, overall efficiency, the solar-to-exergy conversion ratio and the outlet air temperature are defined as the thermal performance indicators of the TLIRS system.

The total energy conservation equation for the storage system after a charging and discharging cycle is:

$$\left(Q_{ch,outlet} + Q_{dis,outlet} + Q_{loss} + Q_{remained} + Q_{fan,ch} + Q_{fan,dis}\right) / \left(Q_{input} + Q_{fan,ch} + Q_{fan,dis}\right) = 1 \tag{33}$$

The amount of heat carried by the outlet air in the charging stage:

$$Q_{ch,outlet} = \int_0^{t_{ch}}\int_{T_0}^{T_{outlet,f}}\dot{m}_{ch}c_{p,f}\mathrm{d}T\mathrm{d}t \tag{34}$$

The amount of heat carried by the outlet air in the discharging stage:

$$Q_{dis,outlet} = \int_0^{t_{dis}} \int_{T_0}^{T_{outlet,f}} \dot{m}_{dis} c_{p,f} dT dt \quad (35)$$

The heat loss at insulation walls of the layer of rocks in one cycle:

$$Q_{loss} = \int_0^{t_{ch}+t_{dis}} \int_0^{H_3} 2\pi R_2 U_w (T_f - T_\infty) dz dt \quad (36)$$

The equavilent thermal energy consumption by the fan in one cycle:

$$Q_{fan} = \left(\int_0^t \int_0^H \left| \frac{dp}{dz} \right| \frac{\dot{m}}{\rho_f} dz dt \right) / (\eta_{fan} \cdot \eta_{CSP}) \quad (37)$$

Here, the derivative of the pressure versus height in the packed bed (d*p*/d*z*) refers to the Ergun equation [63] modified with a buoyancy term [64].

The input heat to the layer pf rocks in the charging stage:

$$Q_{input} = \int_0^{t_{ch}} \int_{T_0}^{T_{outlet,pc}} \dot{m}_{ch} c_{p,f} dT dt \quad (38)$$

The amount of absorbing heat of top layer in the charging stage:

$$Q_{absorb} = \int_0^{t_{ch}} \pi R_2^2 q_{absorb} dt \quad (39)$$

The amount of heat stored in the packed bed in charging stage (energy stored in the air is neglected because it occupies only a very small fraction of the total amount of stored heat):

$$Q_{stored} = \int_0^{H_3} \pi R_2^2 (1-\varepsilon) \rho_s c_{p,s} (T_s - T_{s,pre}) dz \quad (40)$$

Considering the heat losses at insulation walls and by fan power consumption, the absorbing efficiency, charging efficiency, discharging efficiency, overall efficiency, the solar-to-exergy conversion ratio and the outlet air temperature are given by Eqs. (41)–(46):

$$\eta_{absorb} = Q_{absorb} / \left(\dot{Q}_{inc} \cdot t_{ch} \right) \quad (41)$$

$$\eta_{ch} = Q_{stored} / \left(Q_{input} + Q_{fan,ch} \right) \quad (42)$$

$$\eta_{dis} = Q_{dis,outlet} / \left(Q_{stored} + Q_{fan,dis} \right) \quad (43)$$

$$\eta_{overall} = Q_{dis,outlet} / \left(Q_{input} + Q_{fan,ch} + Q_{fan,dis} \right) \quad (44)$$

$$\xi = \frac{\int_0^{t_{dis}} \left(\int_{T_0}^{T_{outlet,f}} \dot{m}_{dis} c_{p,f} dT \right) (1 - T_\infty / T_{outlet}) dt}{\dot{Q}_{inc} \cdot t_{ch} + Q_{fan,ch} + Q_{fan,dis}} \quad (45)$$

$$\overline{T}_{outlet} = \left(\int_0^{t_{dis}} T_{outlet} dt \right) / t_{dis} \quad (46)$$

The models of the TLIRS system are now established. The numerical calculation process is then conducted by the in-house Matlab program.

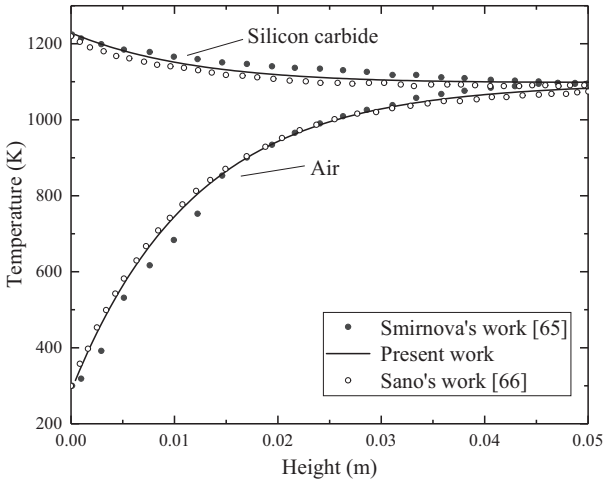

Figure 3. Comparison of two-phase temperature distribution between simulation results and literature results.

Table 4. Main parameters

Main parameters			
β **(m^{-1})**	**501**	m_c **(kg m^{-2} s^{-1})**	**1.2**
ε (–)	0.5	ρ_f (kg m^{-3})	1.2
H (m)	0.07	T_∞ (K)	300
c_p (J kg^{-1} K^{-1})	1000	Radiation (W m^{-2})	10^6
h_v (W m^{-3} K^{-1})	8.8×10^4	k (W m^{-1} K^{-1})	150
$h_{v\text{-top}}$ (W m^{-3} K^{-1})	0		

RESULTS AND DISCUSSION

Model validation

Heat transfer models for the cavity receiver and for the packed bed of rocks have been validated in our previous work [30, 43]. In this paper, we focus on demonstrating the validity of the model for the porous ceramic layer.

The case of a numerical study based on COMSOL for the volumetric solar receiver by Smirnova *et al.* [65] is used for the model validation, the difference between numerical results and literature results for two-phase axial temperature distribution are shown in Fig. 3. Main parameters [65] are given in Table 4. Their high-temperature silicon carbide receiver is exposed to the flux that the density is up to 1000 MW/m^2 by using solar tower technology. The air heated up to temperature of 800°C is used for the steam generator of a steam turbine to generate electricity. The porosity of the porous ceramic is 0.5 [66], and the air mass flow rate is 1.2 kg m^{-2} s^{-1}. Sano *et al.* [66] used the same literature results for model validation and their verification results were also added in Fig. 3 for comparison. A comparison of simulation and literature results shows that the relative errors between the present model and other two numerical models are both less than 5%. The difference in the three sets of curves was found negligible, which confirms that the present local thermal nonequilibrium model is effective and valid.

Porous ceramic layer

First, the temperature distribution and the absorbing efficiency in the porous ceramic layer are discussed.

Fig. 4 shows the temperature difference of the porous ceramic and air, ($T_{pc} - T_f$), with height under different air mass flow rates. The temperature difference decreases with the increase of height.

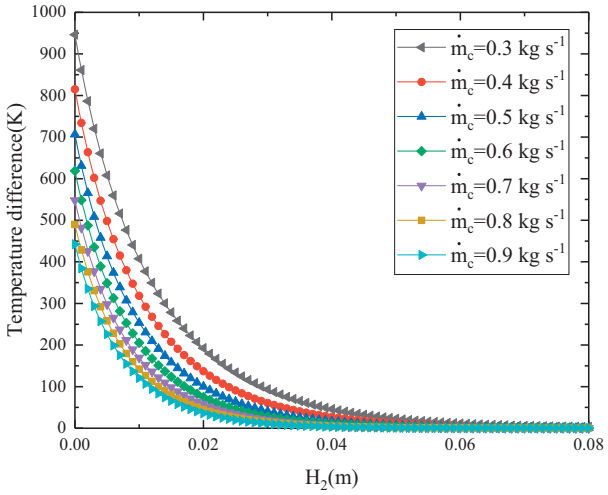

Figure 4. Temperature difference varying with height at different air mass flow rates.

For the same height, the temperature difference can be reduced by increasing the air mass flow rate. For example, the temperature difference at the surface of the porous ceramic layer is over 800 K for the air flow rate of 0.4 kg s^{-1}. The value drops below 500 K as the flow rate increases to 0.8 kg s^{-1}. In addition, increasing the air flow rate also has the effect on shortening the height for reaching the local thermal equilibrium, i.e. no temperature difference existed between two phases. The local thermal equilibrium is not reached until the height of 0.08 m for the air flow rate of 0.3 kg s^{-1}. By contrast, the required height is reduced to 0.047 m for the flow rate of 0.9 kg s^{-1}. This is because the convective heat transfer coefficient increases with the mass flow rate, thus enhancing the heat transfer between the air and porous ceramic phases.

The temperature of gas and solid phases at the inlet and outlet of the porous ceramic layer under different mass flow rates are given in Fig. 5. For the gas phase, air temperature changes rapidly between inlet and outlet (Fig. 5a). The outlet temperature reaches to 1247 K, which is four times larger than the inlet temperature (307 K) for the air flow rate of 0.3 kg s^{-1}. The temperature change decreases with the increase of flow rate. For example, the value drops to 438 K when increasing the flow rate to 0.9 kg s^{-1}. For the solid phase, the temperature change of the porous ceramic between the inlet and outlet keeps in a small level (less than 6 K) in the whole range of air flow rates (Fig. 5b). The solid phase temperature decreases from 1122 K to 795 K when the flow rate increases from 0.4 kg s^{-1} to 0.8 kg s^{-1}.

Fig. 6 shows results of the inlet temperature of porous ceramic and the absorbing efficiency at different air mass flow rates. As the air flow rate increases, the inlet temperature of porous ceramic decreases and the absorbing efficiency can be improved. The inlet temperature is 1254 K for the air flow rate of 0.3 kg s^{-1} and reduced to 747 K for 0.9 kg s^{-1}. Meanwhile, the absorbing efficiency increases from 63% to 83%. It is because that cavity radiative heat losses are reduced as the inlet temperature of porous ceramic decreases. However, the increase rate of the absorbing efficiency slows down with the increasing air flow rate. The absorbing efficiency increases by 8% (from 63% to 71%) for the air flow rate varying from 0.3 to 0.4 kg s^{-1}, but only by 1% (from 82% to 83%) for 0.8 to 0.9 kg s^{-1}.

Layer of rocks

Secondly, the thermal characteristics of solid and fluid phases in the domain of the layer of rocks during charging and discharging is discussed. Based on this, the thermal performance is further evaluated.

Thermal characteristics

For the air mass flow rate of 0.4 and 0.2 kg s^{-1} during charging and discharging, the transient thermal performance of the layer of rocks in terms of temperature distribution of air and rocks and thermal efficiencies in 30 cycles is studied.

The axial temperature distribution of rocks and air after charging and discharging of 1, 10, 20 and 30 cycles are shown in Fig. 7. In general, the thermocline is gradually formed in the beds along charging and discharging cycles. Temperatures reach peaks at the top of beds, decrease along heights and finally drop close to the room temperature at the bottom. For the charging stage (Fig. 7a), maximum temperatures after different cycles are close to 1110 K found at $H_3 = 0$ m. Because heat is transferred from hot air to rocks, air temperature is slightly higher than that of rocks for the same height. With the increase of the number of cycles, temperatures of whole beds increase. For example, the temperature of rocks (air) at $H_3 = 4$ m reaches to 327 K (330 K), 433 K (439 K) and 525 K (531 K), respectively, after charging of 10, 20 and 30 cycles. For the discharging stage (Fig. 7b), the temperature at the top of beds increases while the cyclical charging and discharging proceed. It has increased by 1.4 times (from 690 K to 954 K) after the discharging of 10 cycles compared with the first one. Further increasing the number of cycles, the increase rate drops down. Finally, the temperature at the top of beds climes up to 1016 K at the end of 30 cycles. In addition, contrary to the charging stage, the temperature of rocks is slightly higher than that of air for the same height due to the reverse direction of air flow.

Thermal performance

Fig. 8 shows different thermal efficiencies of the layer of rocks varying with the number of cycles. The charging efficiency maintains at a high level of more than 99% with little change throughout. The evolutions are similar with respect to the discharging efficiency and the overall efficiency. Increases are found rapidly at the beginning and then decrease with cycling. The efficiencies finally reach their maximums of 93% (discharging) and 92% (overall) after 30 cycles. The solar-to-exergy conversion ratio also increases when the number of cycles increases, reaching a plateau after 20 cycles. The final value is up to 46% at the end of cycles.

Fig. 9 illustrates the charging and discharging efficiencies varying with the number of cycles for different air mass flow rates. In general, as the number of cycles increases, the discharging efficiency increases monotonically, while the charging efficiency increases first and then decreases. At the initial stage (first cycle), the charging efficiency increases with air flow rates which can be improved from 99.3% to 99.7% by increasing the flow rate from 0.3 to 0.9 kg s^{-1}. After five cycles, charging efficiencies in different flow rates begin to drop down from their peaks. In addition, as the flow rate increases, the decrease of charging efficiency along cycles is gradually increased. After 30 of cycles, the charging efficiencies in the flow rates of 0.3 and 0.9 kg s^{-1} drop to 99.3% and 98.4%, respectively. By contrast, the discharging efficiency change is much more significant during the whole cycles, e.g. from 60% to 90% in the air flow rate of 0.3 kg s^{-1}. For any stage of cycles, the discharging efficiency always increases with the increase of air flow rates. After 30 of cycles, for example, the discharging

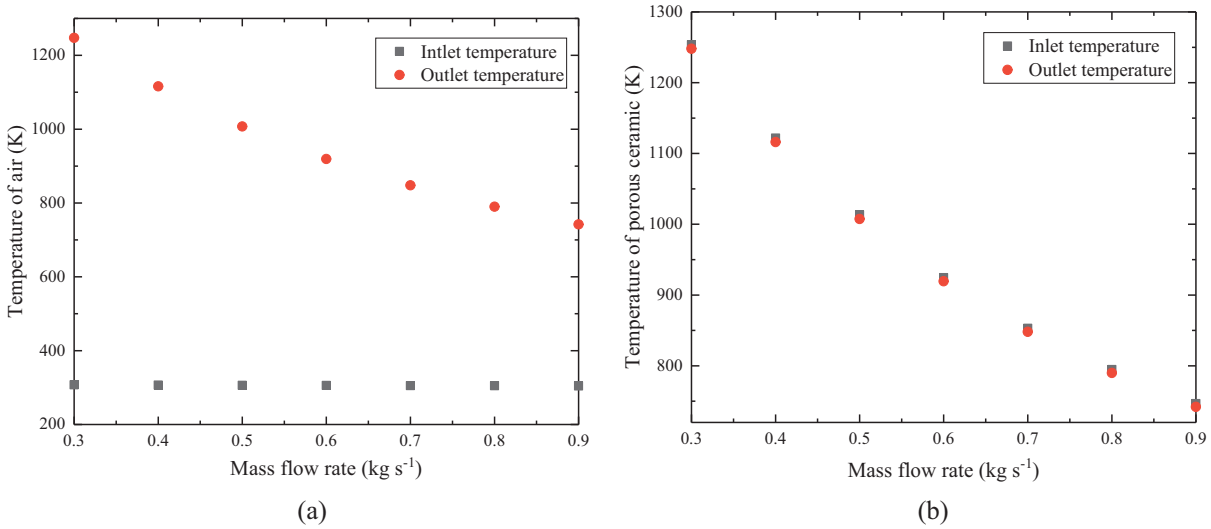

Figure 5. Temperature of (a) gas phase: Air and (b) solid phase: Porous ceramic, at the inlet and outlet of the porous ceramic layer varying with air mass flow rate.

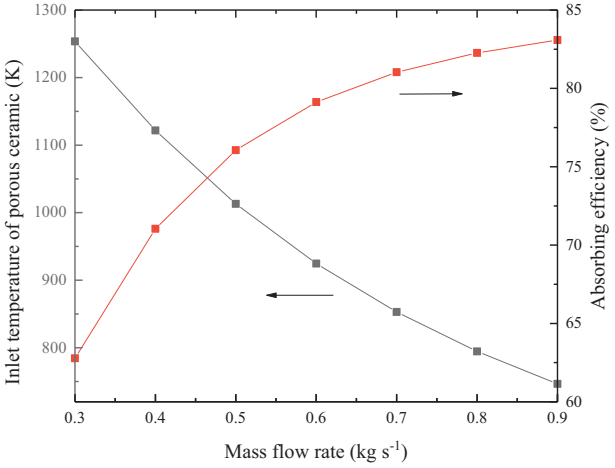

Figure 6. Inlet temperature of porous ceramic and absorbing efficiency varying with air mass flow rate.

efficiencies are 94%, 96% and 97% corresponding to the air flow rates in 0.5, 0.7 and 0.9 kg s^{-1}.

Fig. 10 shows results of the overall efficiency and solar-to-exergy conversion ratio varying with the number of cycles for different air mass flow rates. In general, as the number of cycles increases, the overall efficiency and solar-to-exergy conversion ratio increase monotonically. At the initial stage (first cycle), overall efficiencies are low generally. Maximum rates of overall efficiencies are found at the beginning which drop down with the number of cycles. During 30 cycles, overall efficiencies finally climes from 60% up to 90% in the air flow rate of 0.3 kg s^{-1}. For any stage of cycles, overall efficiencies always increase by increasing the air flow rate. After 30 cycles, the overall efficiency approaches 90%, 94% and 96% corresponding to e air flow rates of 0.3, 0.6 and 0.9 kg s^{-1}. In addition, similar variation trends are found with respect to solar-to-exergy conversion ratios varying with cycles and air flow rates. For example, the initial solar-to-exergy ratio is less than 0.25, which can eventually approach to 0.41, in the air flow rate of 0.3 kg s^{-1}. This value can be further increased to 0.49 by increasing the air flow rate to 0.6 kg s^{-1}.

The outlet air temperature at the 15th and 30th cycles varying with discharging time for different charging air mass flow rates are shown in Fig. 11. On one hand, outlet air temperatures drop gradually over discharging time for the whole range of air mass flow rates. A lower charging air flow rate leads to a higher average outlet air temperature and a larger temperature drop. For example, after the 30th cycle, the average outlet air temperature and temperature drop are 1158 K and 94 K respectively for the charging air flow rate of 0.3 kg s^{-1}, which turn to 725 K and 51 K for the flow rate of 0.9 kg s^{-1}. On the other hand, the decline of outlet air temperature can be improved by increasing cycles. For the air flow rate of 0.5 kg s^{-1}, the outlet air temperature drop decreases from 106 K to 78 K at the end of 30th cycle compared with that after 15 cycles.

Comparison of storage systems

Comparison of the TLIRS and SLIRS systems

The TLIRS was then compared with the previous SLIRS system. Using the same parameters of dimensions and operation conditions as the TLIRS system (Table 1) with a fixed air mass flow rate of 0.4 kg s^{-1}, thermal performance of the two systems in 30 cycles was assessed.

Fig. 12 shows the axial solid temperature distribution of two systems after 10, 20 and 30 cycles. In general, along the height, the profile of solid temperature decreases from the peak value at the top of beds to the room temperature at the bottom. The maximum temperatures after 30 cycles approach to 925 K and 1317 K, found at $H_3 = 0$ m, for the TLIRS and SLIRS systems. The solid temperature of the SLIRS system drops much more sharply (by 451 K) than that of the TLIRS system (by only 7 K) in the height range of 0 to 0.1 m. For the height over 0.1 m, the solid temperature of the TLIRS system is higher than that of the TLIRS system all the time that is because the TLIRS system can transport the intensive solar energy into beds more effectively due to the enhanced radiative heat transfer by using the porous ceramic layer. The solid temperature at the top decreases to a large extent so that the radiation losses from receiver to the surroundings are reduced. As a result, the improved utilization of thermal energy leads to the overall increase of the axial temperature of beds. For example, the solid temperature of the TLIRS system and SLIRS

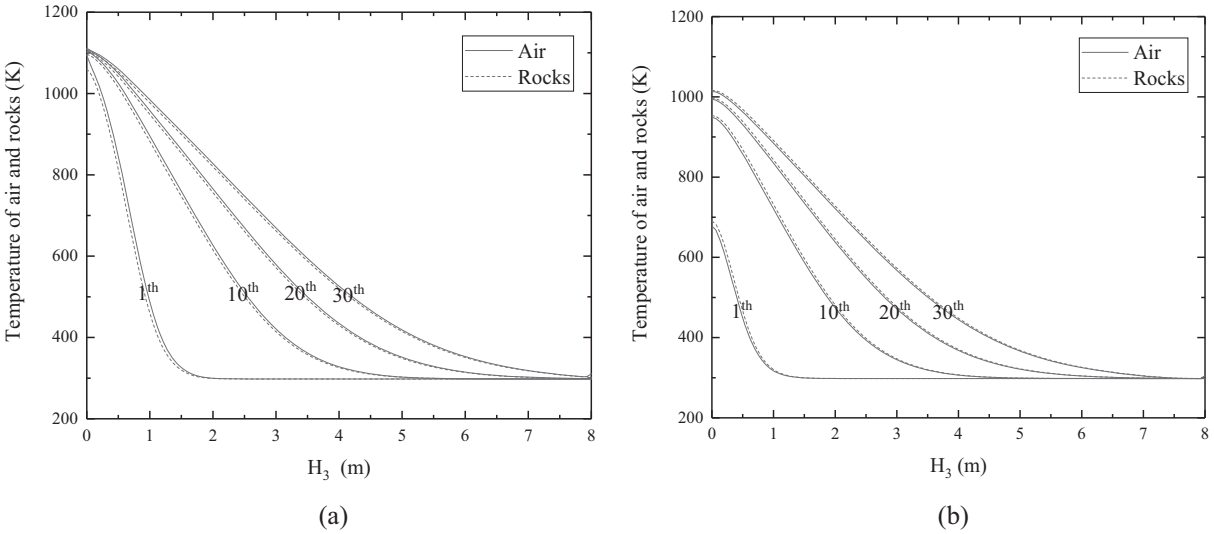

Figure 7. Axial temperature distribution of air and rocks after the (a) charging and (b) discharging of 1, 10, 20 and 30 cycles.

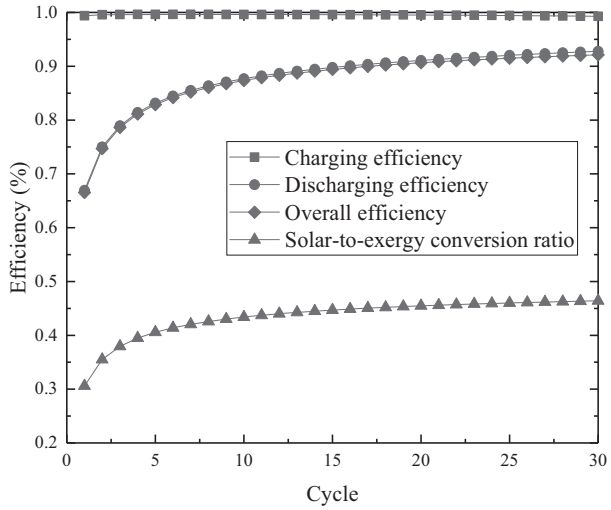

Figure 8. Thermal efficiencies of the layer of rocks in 30 cycles.

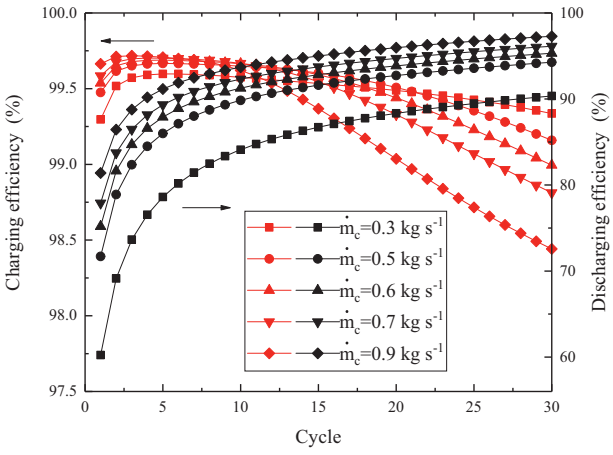

Figure 9. Charging and discharging efficiencies varying with the number of cycles for different air mass flow rates.

Table 5. Comparison of the TLIRS system to the SLIRS system

system	$\overline{T}_{outlet}$(K)	η_{absorb} (%)	η_{ch}(%)	η_{dis}(%)	$\eta_{overall}$(%)	ξ (–)
TLIRS	569	79.1	99.0	95.3	94.4	0.49
SLIRS	526	72.0	98.9	95.8	94.8	0.44

system at $H_3 = 4$ m reaches to 363 K (345 K), 467 K (427 K) and 534 K (482 K), respectively, after 10, 20 and 30 cycles.

Table 5 illustrates the comparison of thermal performance between the TLIRS system to the SLIRS system after 30 cycles. According to Eq. (41), the absorbing efficiency is defined as the ratio of absorbing heat of top layer to the incident radiation in the charging stage. It is worth noting that the absorbing heat of top layer decreases monotonously with solid temperature in the studied range. The solid temperature at the top position of the TLIRS system (925 K) is lower than that of the SLIRS system (1317 K), which makes the TLIRS system enable to achieve a higher absorbing efficiency (79.1%) than the SLIRS system (72%). The average outlet air temperature of the TLIRS system is higher because utilization of thermal energy in TLIRS system is improved by porous ceramic layer, leading to the overall increase of the axial temperature (including the outlet air temperature). Meanwhile, the higher outlet air temperature leads to the larger solar-to-exergy conversion ratio of 0.49 for the TLIRS system, which is of 0.44 for the SLIRS system. In general, the TLIRS system has better thermal performance compared with the SLIRS system.

Comparison of the TLIRS system to CSP storage plants

The thermal performance of the TLIRS system is compared with existing CSP storage plants using the single-tank packed bed: Solar One in California [67, 68], the 100 MWh_{th} TES system in Ait Baha [69, 70] and the CSPonD in Masdar [13, 71]. Under the similar average outlet air temperature, absorbing efficiency, charging efficiency, discharging efficiency, overall efficiency and the solar-to-exergy conversion ratio are taken as thermal performance indicators.

Table 6 depicts the comparison of thermal performance between the TLIRS system and CSP storage plants. It is clear that when the average outlet air temperature is all around 830 K, the

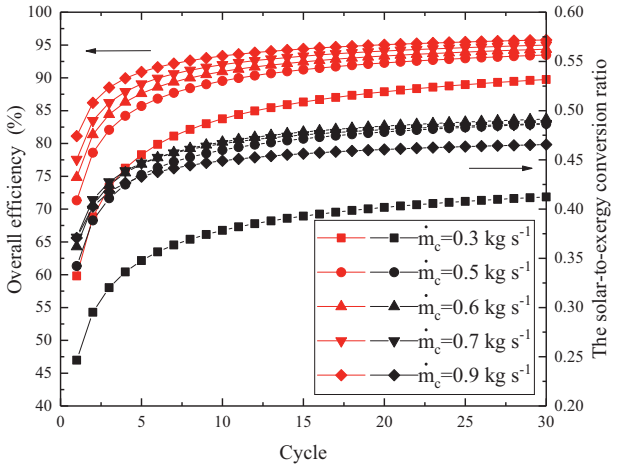

Figure 10. Overall efficiency and solar-to-exergy conversion ratio varying with the number of cycles for different air mass flow rates.

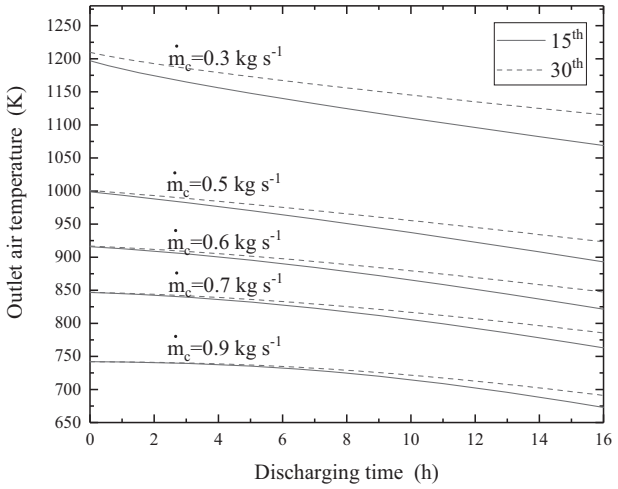

Figure 11. Outlet air temperature at the 15th and 30th cycles varying with discharging time for different charging air mass flow rates.

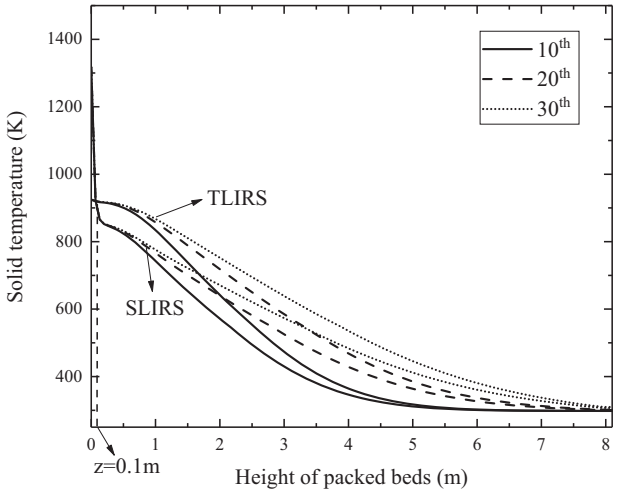

Figure 12. Axial solid temperature distribution of the TLIRS system and SLIRS system after 10, 20 and 30 cycles.

TLIRS system has higher absorbing efficiency, charging efficiency, discharging efficiency, overall efficiency and the solar-to-exergy conversion ratio.

Table 6. Comparison of the TLIRS system to CSP storage plants

system	$\bar{T}_{outlet}$(K)	η_{absorb} (%)	η_{ch}(%)	η_{dis}(%)	$\eta_{overall}$(%)	ξ (–)
TLIRS	822	79	99	96	95	0.49
Ait Baha	833	77	98	91	89	0.46
CSPond	823	75			95.5	0.48
Solar One	839	69			90	0.42

CONCLUSIONS

A TLIRS system for a beam-down CSP system was prosed and analyzed in this paper. The structure of the TLIRS consists of a cavity receiver and packed bed storage with two layers (a porous ceramic layer and a layer of rocks). The porous ceramic layer is set on the top of packed bed to strengthen the inner heat transfer and the second layer of rocks functions as sensible heat storage. We analyzed the thermal performance of these two layers and compared the TLIRS system with a SLIRS system and a CSP storage systems.

Under the set solar irradiance and concentration ratio, the results indicate that the mass flow rate plays an important role in the thermal performance of the TLIRS system. An appropriate mass flow rate can be selected according to the designed temperature value of the downstream application. The porous ceramic layer in the TLIRS system significantly enhances internal heat transfer and effectively improves the absorbing efficiency and outlet air temperature. Compared with a SLIRS system, the absorbing efficiency and average outlet air temperature of the TLIRS system were improved by 7.1% and 45 K with an air mass flow rate of 0.4 kg s^{-1} after 30 cycles. At similar outlet air temperature, the TLIRS system for beam-down CSP system reached better thermal performance than existing CSP storage plants using the single-tank packed bed with an absorbing efficiency of 79%, 99% charging efficiency, 96% discharging efficiency, 95% overall efficiency and a solar-to-exergy conversion ratio of 0.49.

Author contributions

Xiuxiu Li: data curation, formal analysis, investigation, methodology, software, validation, writing—original draft, writing—review and editing.

Song Yang: conceptualization, project administration, resources, software, supervision, validation, writing—review and editing.

Jun Wang: funding acquisition, project administration, resources, supervision.

Peter D. Lund: project administration, resources, software, supervision, writing—review and editing.

Conflict of interest

The authors declare that they have no known competing financial interests or personal relationships that could have appeared to influence the work reported in this paper.

Data availability statement and funding

All data included in this study are available upon request by contact with the corresponding author.

Acknowledgements

This research has been supported by National Natural Science Foundation of China (grant 22109022).

References

1. Palacios A, Barreneche C, Navarro ME, Ding Y. Thermal energy storage technologies for concentrated solar power – a review from a materials perspective. *Renew Energy*. 2020;**156**:1244–65. https://doi.org/10.1016/j.renene.2019.10.127
2. Peinado Gonzalo A, Pliego Marugán A, García Márquez FP. A review of the application performances of concentrated solar power systems. *Appl Energy*. 2019;**255**:113893. https://doi.org/10.1016/j.apenergy.2019.113893
3. Pelay U, Luo L, Fan Y *et al.* Thermal energy storage systems for concentrated solar power plants. *Renew Sust Energ Rev*. 2017;**79**: 82–100. https://doi.org/10.1016/j.rser.2017.03.139
4. Tao YB, He YL. A review of phase change material and performance enhancement method for latent heat storage system. *Renew Sust Energ Rev*. 2018;**93**:245–59. https://doi.org/10.1016/j.rser.2018.05.028
5. Jiang K, Du X, Kong Y *et al.* A comprehensive review on solid particle receivers of concentrated solar power. *Renew Sust Energ Rev*. 2019;**116**:109463. https://doi.org/10.1016/j.rser.2019.109463
6. Yu Q, Li X, Wang Z, Zhang Q. Modeling and dynamic simulation of thermal energy storage system for concentrating solar power plant. *Energy*. 2020;**198**:117183. https://doi.org/10.1016/j.energy.2020.117183
7. Thanganadar D, Fornarelli F, Camporeale S *et al.* Thermo-economic analysis, optimisation and systematic integration of supercritical carbon dioxide cycle with sensible heat thermal energy storage for CSP application. *Energy*. 2022;**238**:121755. https://doi.org/10.1016/j.energy.2021.121755
8. Tang N, Zhang Y, Niu Y, Du X. Solar energy curtailment in China: status quo, reasons and solutions. *Renew Sust Energ Rev*. 2018;**97**: 509–28. https://doi.org/10.1016/j.rser.2018.07.021
9. Zhang Q, Cao D, Jiang K *et al.* Heat transport characteristics of a peak shaving solar power tower station. *Renew Energy*. 2020;**156**:493–508. https://doi.org/10.1016/j.renene.2020.04.099
10. El Alami, Asbik M, Agalit H. Identification of natural rocks as storage materials in thermal energy storage (TES) system of concentrated solar power (CSP) plants – a review. *Sol Energy Mater Sol Cells*. 2020;**217**:110599. https://doi.org/10.1016/j.solmat.2020.110599
11. Awan AB, Zubair M, Chandra Mouli KVV. Design, optimization and performance comparison of solar tower and photovoltaic power plants. *Energy*. 2020;**199**:117450. https://doi.org/10.1016/j.energy.2020.117450
12. Collado FJ, Guallar J. A review of optimized design layouts for solar power tower plants with campo code. *Renew Sust Energ Rev*. 2013;**20**:142–54. https://doi.org/10.1016/j.rser.2012.11.076
13. Slocum AH, Codd DS, Buongiorno J *et al.* Concentrated solar power on demand. *Sol Energy*. 2011;**85**:1519–29. https://doi.org/10.1016/j.solener.2011.04.010
14. Rabl A. Tower reflector for solar power plant. *Sol Energy*. 1976;**18**: 269–71. https://doi.org/10.1016/0038-092X(76)90027-X
15. Yogev A, Kribus A, Epstein M. Solar "tower reflector" systems : a new approach solar plants. *Int J Hydrog Energy*. 1998;**23**:239–45. https://doi.org/10.1016/S0360-3199(97)00059-1
16. Segal A, Epstein M. The optics of the solar tower reflector. *Sol Energy*. 2001;**69**:229–41. https://doi.org/10.1016/s0038-092x(00)00137-7
17. Epstein M, Olalde G, Santén S *et al.* Towards the industrial solar carbothermal production of zinc. *J Sol Energy Eng*. 2008;**130**: 0145051–4. https://doi.org/10.1115/1.2807214
18. Yadav D, Banerjee R. A review of solar thermochemical processes. *Renew Sust Energ Rev*. 2016;**54**:497–532. https://doi.org/10.1016/j.rser.2015.10.026
19. Hasuike H, Yoshizawa Y, Suzuki A, Tamaura Y. Study on design of molten salt solar receivers for beam-down solar concentrator. *Sol Energy*. 2006;**80**:1255–62. https://doi.org/10.1016/j.solener.2006.03.002
20. Li X, Dai YJ, Wang RZ. Performance investigation on solar thermal conversion of a conical cavity receiver employing a beam-down solar tower concentrator. *Sol Energy*. 2015;**114**:134–51. https://doi.org/10.1016/j.solener.2015.01.033
21. Matsubara K, Kazuma Y, Sakurai A *et al.* High-temperature fluidized receiver for concentrated solar radiation by a beam-down reflector system. *Energy Procedia*. 2014;**49**:447–56. https://doi.org/10.1016/j.egypro.2014.03.048
22. Matsubara K, Sakai H, Kazuma Y *et al.* Numerical modeling of a two-tower type fluidized receiver for high temperature solar concentration by a beam-down reflector system. *Energy Procedia*. 2015;**69**:487–96. https://doi.org/10.1016/j.egypro.2015.03.057
23. Nakakura M, Ohtake M, Matsubara K *et al.* Development of a receiver evaluation system using 30 kWth point concentration solar simulator. *Energy Procedia*. 2015;**69**:497–505. https://doi.org/10.1016/j.egypro.2015.03.058
24. Thalange VC, Pal E, Minocha N *et al.* Thermal hydraulics of natural circulation loop in beam-down solar power tower. *Energy*. 2018;**159**:1088–101. https://doi.org/10.1016/j.energy.2018.06.156
25. Yang S, Li L, Wang B *et al.* Thermodynamic analysis of a conceptual fixed-bed solar thermochemical cavity receiver–reactor Array for water splitting via ceria redox cycling. *Front Energy Res*. 2021;**9**. https://doi.org/10.3389/fenrg.2021.565761
26. Kiwan S, Soud QR. Numerical investigation of sand-basalt heat storage system for beam-down solar concentrators. *Treaties and other international acts series*. 2019;**13**:100372. https://doi.org/10.1016/j.csite.2018.100372
27. Shao S *Performance optimization study of the tower reflector solar power system*. Nanjing Normal University, 2020
28. Grange B, Kumar V, Gil A *et al.* Preliminary optical, thermal and structural design of a 100 kWth CSPonD beam-down on-sun demonstration plant. *Energy Procedia*. 2015;**75**:2163–8. https://doi.org/10.1016/j.egypro.2015.07.359
29. Yang S, Wang J, Lund PD *et al.* Modelling and performance evaluation of an integrated receiver-storage for concentrating solar power beam-down system under heterogeneous radiative conditions. *Sol Energy*. 2019;**188**:1264–73. https://doi.org/10.1016/j.solener.2019.07.031
30. Yang S, Wang J, Lund PD *et al.* High performance integrated receiver-storage system for concentrating solar power beam-down system. *Sol Energy*. 2019;**187**:85–94. https://doi.org/10.1016/j.solener.2019.05.041
31. Calvet N, Slocum AH, Gil A *et al.* Dispatchable solar power using molten salt directly irradiated from above. *Sol Energy*. 2021;**220**: 217–29. https://doi.org/10.1016/j.solener.2021.02.058
32. Barreto G, Canhoto P, Collares-Pereira M. Three-dimensional CFD modelling and thermal performance analysis of porous volumetric receivers coupled to solar concentration systems. *Appl Energy*. 2019;**252**:113433. https://doi.org/10.1016/j.apenergy.2019.113433
33. Hammel EC, Ighodaro OLR, Okoli OI. Processing and properties of advanced porous ceramics: an application based review. *Ceram Int*. 2014;**40**:15351–70. https://doi.org/10.1016/j.ceramint.2014.06.095

34. Chen X, Xia XL, Meng XL, Dong XH. Thermal performance analysis on a volumetric solar receiver with double-layer ceramic foam. *Energy Convers Manag*. 2015;**97**:282–9. https://doi.org/10.1016/j.enconman.2015.03.066
35. Scale-integrated simulation of coupled radiation and convection in metal foam layer under high-flux irradiation. *Int J Heat Mass Transf*. 2020;**150**:119367. https://doi.org/10.1016/j.ijheatmasstransfer.2020.119367
36. Zaversky F, Aldaz L, Sánchez M *et al.* Numerical and experimental evaluation and optimization of ceramic foam as solar absorber – single-layer vs multi-layer configurations. *Appl Energy*. 2018;**210**:351–75. https://doi.org/10.1016/j.apenergy.2017.11.003
37. Agrafiotis CC, Mavroidis I, Konstandopoulos AG *et al.* Evaluation of porous silicon carbide monolithic honeycombs as volumetric receivers/collectors of concentrated solar radiation. *Sol Energy Mater Sol Cells*. 2007;**91**:474–88. https://doi.org/10.1016/j.solmat.2006.10.021
38. Zanganeh G, Khanna R, Walser C *et al.* Experimental and numerical investigation of combined sensible-latent heat for thermal energy storage at 575°C and above. *Sol Energy*. 2015;**114**:77–90. https://doi.org/10.1016/j.solener.2015.01.022
39. Xu C, Liu DY, Zheng Y, Lü JH. Research on porous media receiver heat transfer of solar power tower plant, Zhongguo Dianji Gongcheng Xuebao/proceedings Chinese Soc. *Electr Eng*. 2010;**30**:117–22. https://doi.org/10.13334/j.0258-8013.pcsee.2010.20.016
40. Kelley KK *High-temperature heat-content, heat-capacity, and entropy data for the elements and inorganic compounds*. US Bureau of Mines Bull, Elsevier, 1960
41. Somerton WH *Thermal Properties and Temperature-Related Behavior of Rock/Fluid Systems*. Elsevier, 1992
42. Zanganeh G, Pedretti A, Zavattoni S *et al.* Packed-bed thermal storage for concentrated solar power - pilot-scale demonstration and industrial-scale design. *Sol Energy*. 2012;**86**:3084–98. https://doi.org/10.1016/j.solener.2012.07.019
43. Yang S, Wang J, Lund PD *et al.* Design and performance evaluation of a high-temperature cavity receiver for a 2-stage dish concentrator. *Sol Energy*. 2018;**174**:1126–32. https://doi.org/10.1016/j.solener.2018.10.021
44. ToolBox E *Dry Air Properties*, Elsevier, 2005
45. Furler P, Steinfeld A. Heat transfer and fluid flow analysis of a 4kW solar thermochemical reactor for ceria redox cycling. *Chem Eng Sci*. 2015;**137**:373–83. https://doi.org/10.1016/j.ces.2015.05.056
46. Wang P, Vafai K, Liu DY. Analysis of the volumetric phenomenon in porous beds subject to irradiation. *Numeri Heat Transf A Appl*. 2016;**70**:567–80. https://doi.org/10.1080/10407782.2016.1192941
47. Reddy KS, Nataraj S. Thermal analysis of porous volumetric receivers of concentrated solar dish and tower systems. *Renew Energy*. 2019;**132**:786–97. https://doi.org/10.1016/j.renene.2018.08.030
48. Rosseland S *Theoretical Astrophysics: Atomic Theory and the Analysis of Stellar Atmospheres and Envelopes*. Oxford: Clarendon Press, 1936
49. Lapp J, Davidson JH, Lipiński W. Heat transfer analysis of a solid-solid heat recuperation system for solar-driven nonstoichiometric redox cycles. *J Sol Energy Eng*. 2013;**135**. https://doi.org/10.1115/1.4023357
50. J. Lapp, *Thermal modeling and design of a solar non-stoichiometric redox reactor with heat recovery*, (2013). http://conservancy.umn.edu/handle/11299/159856.
51. Lidor A, Fend T, Roeb M, Sattler C. Parametric investigation of a volumetric solar receiver-reactor. *Sol Energy*. 2020;**204**:256–69. https://doi.org/10.1016/j.solener.2020.04.045
52. Mendes MAA, Talukdar P, Ray S, Trimis D. Detailed and simplified models for evaluation of effective thermal conductivity of open-cell porous foams at high temperatures in presence of thermal radiation. *Int J Heat Mass Transf*. 2014;**68**:612–24. https://doi.org/10.1016/j.ijheatmasstransfer.2013.09.071
53. Keene DJ, Davidson JH, Lipiński W. A model of transient heat and mass transfer in a heterogeneous medium of ceria undergoing nonstoichiometric reduction. *J Heat Transf*. 2013;**135**. https://doi.org/10.1115/1.4023494
54. Lapp J, Lipinski W. Transient three-dimensional heat transfer model of a solar thermochemical reactor for H2O and CO2 splitting via nonstoichiometric ceria redox cycling. *J Sol Energy Eng Trans ASME*. 2014;**136**. https://doi.org/10.1115/1.4026465
55. Hwang GJ, Wu CC, Chao CH. Investigation of non-darcian forced convection in an asymmetrically heated sintered porous channel. *J Heat Transf*. 1995;**117**:725–32. https://doi.org/10.1115/1.2822636
56. Alazmi B, Vafai K. Analysis of variants within the porous media transport models. *J Heat Transf*. 2000;**122**:303–26. https://doi.org/10.1115/1.521468
57. Kunii D, Smith J. Heat transfer characteristics of porous rocks. *AICHE J*. 1960;**6**:71–8. https://doi.org/10.1002/aic.690060115
58. Yagi S, Kunii D. Studies on effective thermal conductivities in packed beds. *AICHE J*. 1957;**3**:373–81. https://doi.org/10.1002/aic.690030317
59. Coutier JP, Farber EA. Two applications of a numerical approach of heat transfer process within rock beds. *Sol Energy*. 1982;**29**:451–62. https://doi.org/10.1016/0038-092X(82)90053-6
60. Alanís E, Saravia L, Rovetta L. Measurement of rock pile heat transfer coefficients. *Sol Energy*. 1977;**19**:571–2. https://doi.org/10.1016/0038-092X(77)90114-1
61. Beek J. Design of Packed Catalytic Reactors. *Adv Chem Eng*. 1962;**3**:203–71. https://doi.org/10.1016/S0065-2377(08)60060-5
62. Ofuchi K, Kunii D. Heat-transfer characteristics of packed beds with stagnant fluids. *Int J Heat Mass Transf*. 1965;**8**:749–57. https://doi.org/10.1016/0017-9310(65)90021-9
63. Ergun S, Orning AA. Fluid flow through randomly packed columns and fluidized beds. *Ind Eng Chem*. 1949;**41**:1179–84. https://doi.org/10.1021/ie50474a011
64. Andersen KT. Theory for natural ventilation by thermal buoyancy in one zone with uniform temperature. *Build Environ*. 2003;**38**:1281–9. https://doi.org/10.1016/S0360-1323(03)00132-X
65. Smirnova O, Fend T, Peter S, Schöllgen D Homogeneous and inhomogeneous model for flow and heat transfer in porous materials as high temperature solar air receivers. In: *Proceedings of the COMSOL Conference*, Vol. **2010**, 2010, 2–6
66. Sano Y, Iwase S, Nakayama A. A local thermal nonequilibrium analysis of silicon carbide ceramic foam as a solar volumetric receiver. *J Sol Energy Eng*. 2012;**134**:3–5. https://doi.org/10.1115/1.4005758
67. Kolb GJ, Alpert DJ, Lopez CW. Insights from the operation of solar one and their implications for future central receiver plants. *Sol Energy*. 1991;**47**:39–47. https://doi.org/10.1016/0038-092X(91)90061-Z
68. Granqvist CG. Insights from the operation of solar one and their implications for future central receiver plants. *Appl Phys A Solids Surfaces*. 1991;**52**:83–93. https://doi.org/10.1007/BF00323721
69. Zanganeh G, Pedretti A, Zavattoni SA *et al.* Design of a 100 MWhth packed-bed thermal energy storage. *Energy Procedia*. 2014;**49**:1071–7. https://doi.org/10.1016/j.egypro.2014.03.116

70. Zanganeh G, Ambrosetti G, Pedretti A *et al*. A 3 MWth parabolic trough CSP plant operating with air at up to 650 °c, in. *International Renewable and Sustainable Energy Conference (IRSEC)*. 2014;**2014**:108–13. https://doi.org/10.1109/IRSEC.2014.7059884

71. A. Gil, B. Grange, V.G. Perez *et al*. *CSPonD demonstrative project: Start-up process of a 25 kW prototype, in: 2017 AIP Confenrence Proceedings, 2017, pp*. 1850. https://doi.org/10.1063/1.4984477.